The Supplementary Information include:

Characterizations of the as-prepared and reduced catalysts

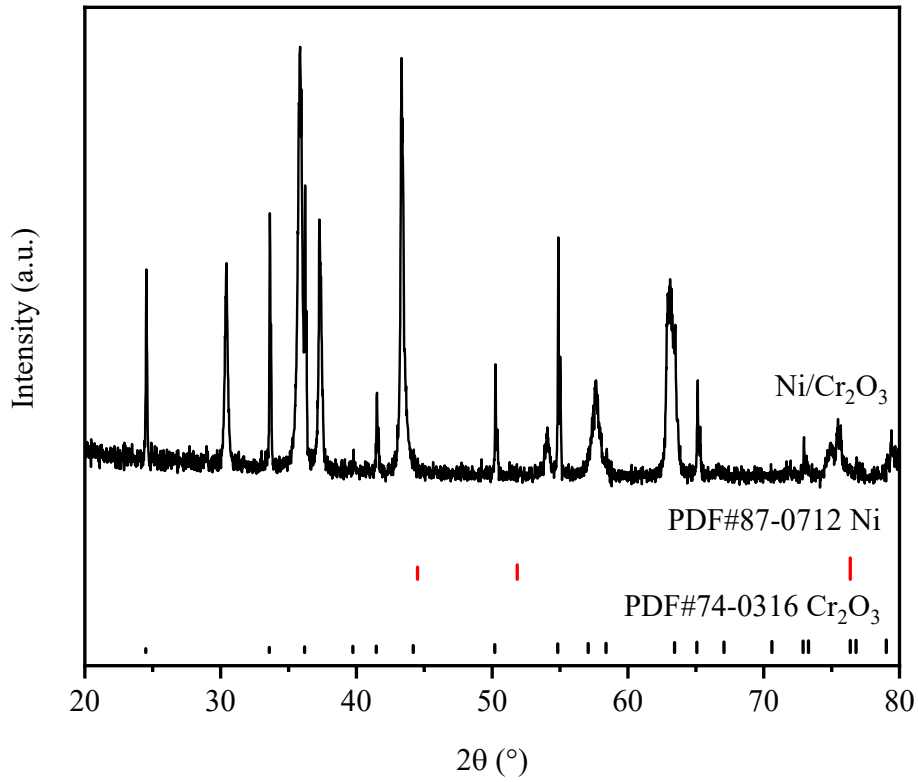

Fig. S1. XRD patterns of the control Ni/Cr_2O_3.

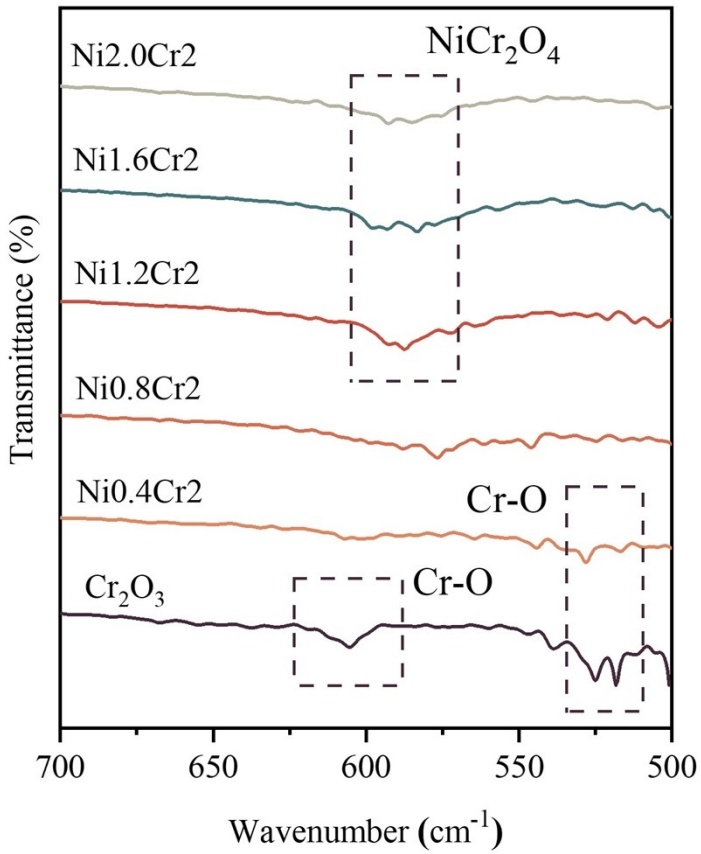

Fig. S2. ATR patterns of the Ni*x*Cr2 catalysts with diffrent Ni/Cr ratios.

For cubic spinel, four infrared vibrations were reported, in which two are located within 600–400 cm^{-1} and the other two that are difficult to be recorded are at low frequencies of 300–200 cm^{-1}. The peak located at approximately 530 cm^{-1} is attributed to the vibration of the Cr-O bond, whereas the peak at 595 cm^{-1} belongs to the characteristic band of the $NiCr_2O_4$ spinel. These results further confirm the generation of $NiCr_2O_4$ spinel oxides under Ni/Cr ratio≥ 0.6 conditions.

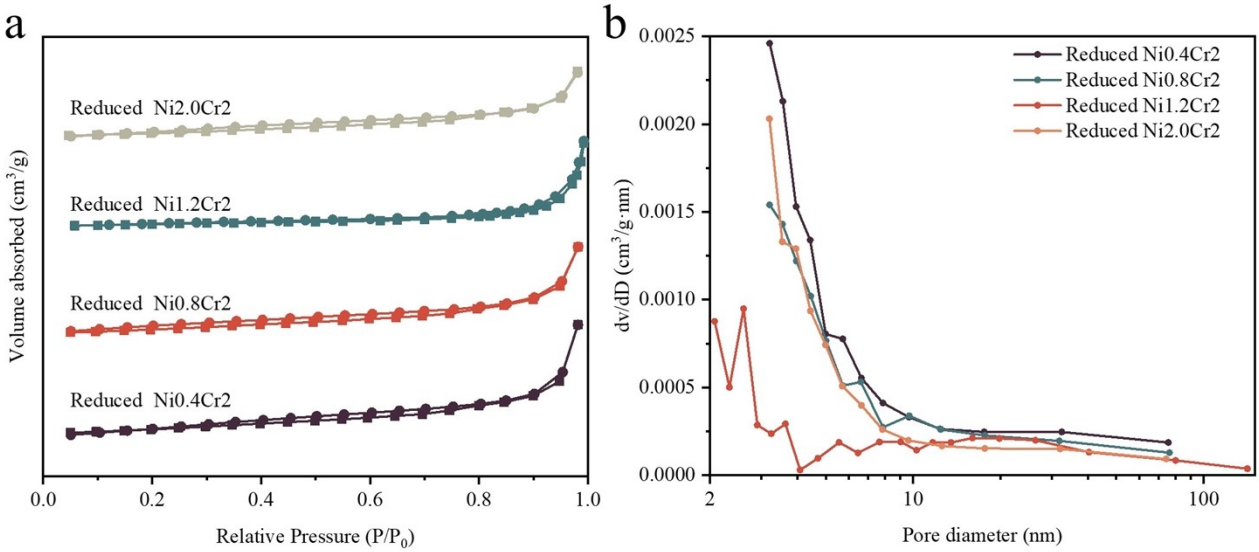

Fig. S3. Physical property analysis a) N_2 adsorption/desorption isotherms of the reduced Ni*x*Cr2 catalysts; b) Pore size distributions of the reduced Ni*x*Cr2 catalysts.

All the samples exhibited isotherms, indicating the mesoporous structure of the hydrogen-reduced $NiCr_2O_4$ catalysts. The BET surface areas, pore size distributions, and pore volumes of the hydrogen-reduced $NiCr_2O_4$ catalysts are summarised in Table S2. Specifically, the increase in the Ni/Cr ratios results in the reduction of their BET surface areas, possibly attributing to the pore structure coverage of $Cr_2O_{3-\delta}$ oxides by Ni.

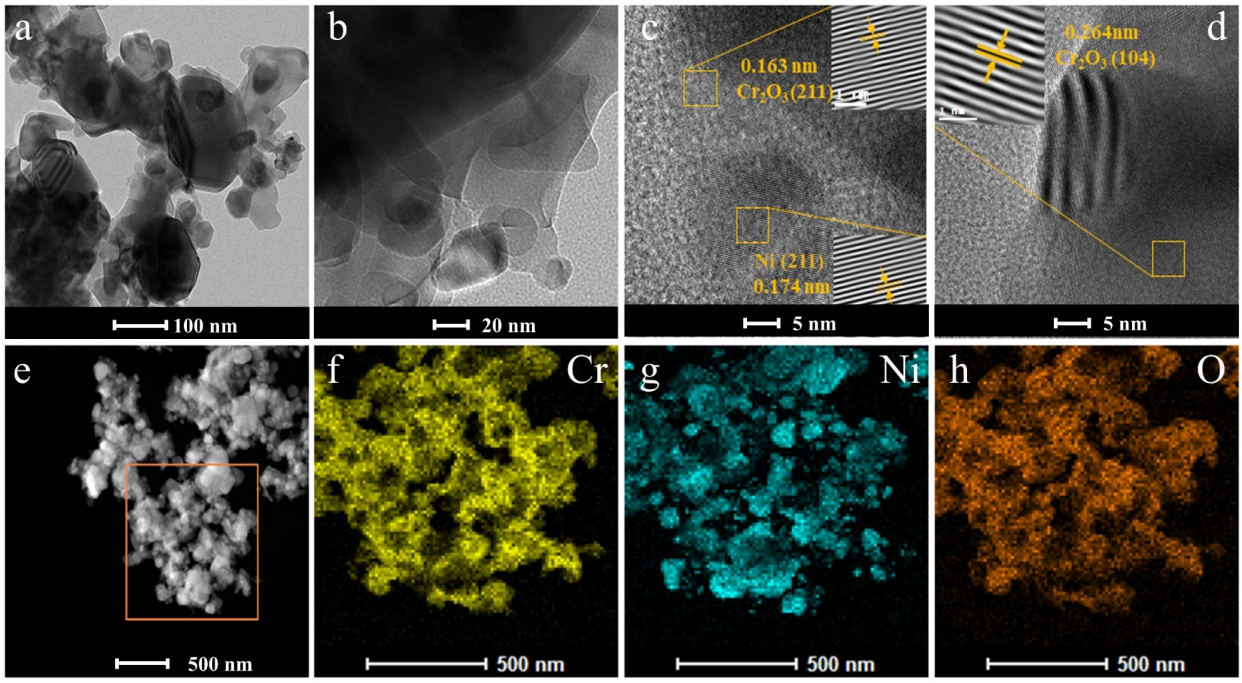

Fig. S4. Morphological characterization of control Ni/Cr_2O_3 a-d) HR-TEM; e-h) EDX mapping results of Cr, Ni, and O elements.

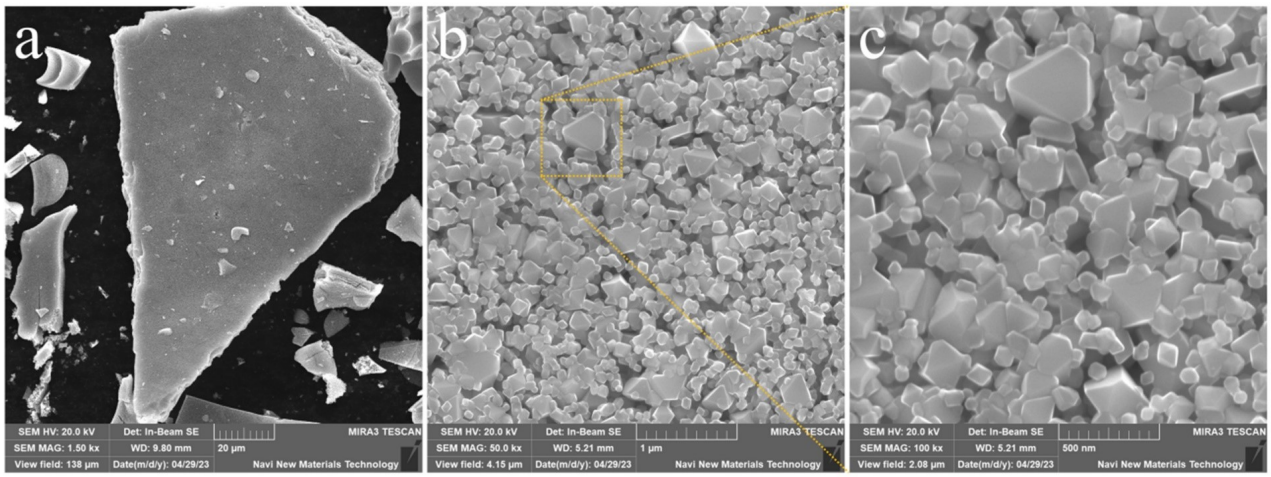

Fig. S5. SEM images of the Ni1.2Cr2.

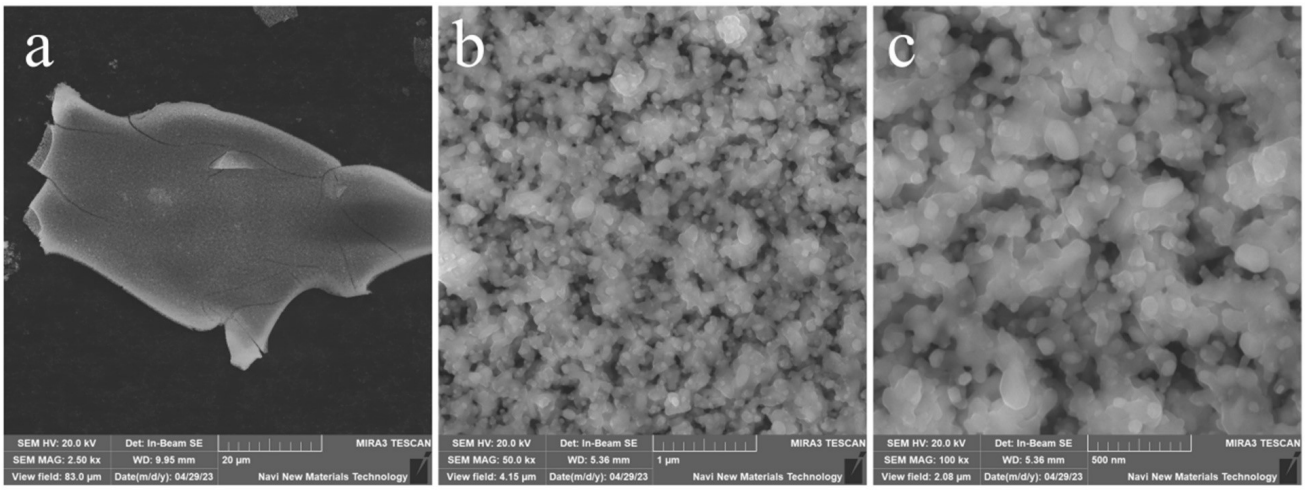

Fig. S6. SEM images of the reduced Ni1.2Cr2.

Catalytic methane decomposition

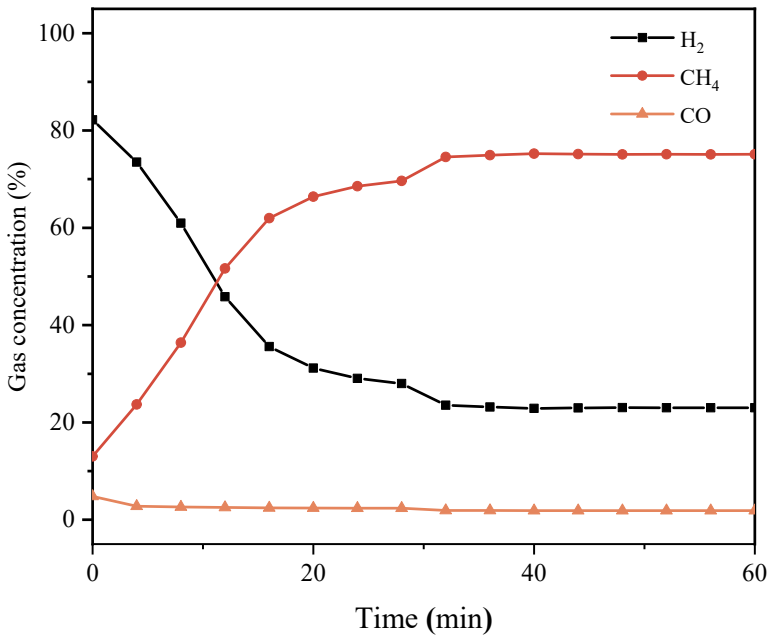

Fig. S7. Evolution of H_2, CH_4, and CO concentrations at 750°C using control group Ni/Cr_2O_3.

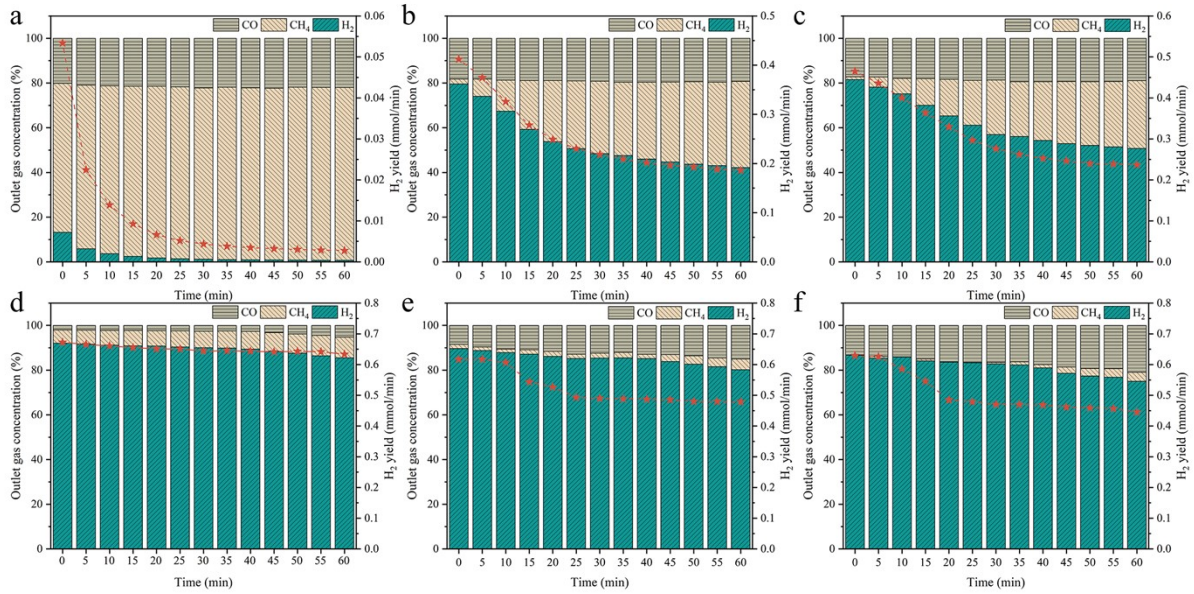

Fig. S8. Outlet gas concentration and H_2 yield of CMD with different Ni/Cr ratios within 60 minutes on a) Cr_2O_3; b) reduced Ni0.4Cr2; c) reduced Ni0.8Cr2; d) reduced Ni1.2Cr2; e) reduced Ni1.6Cr2; f) reduced Ni2.0Cr2.

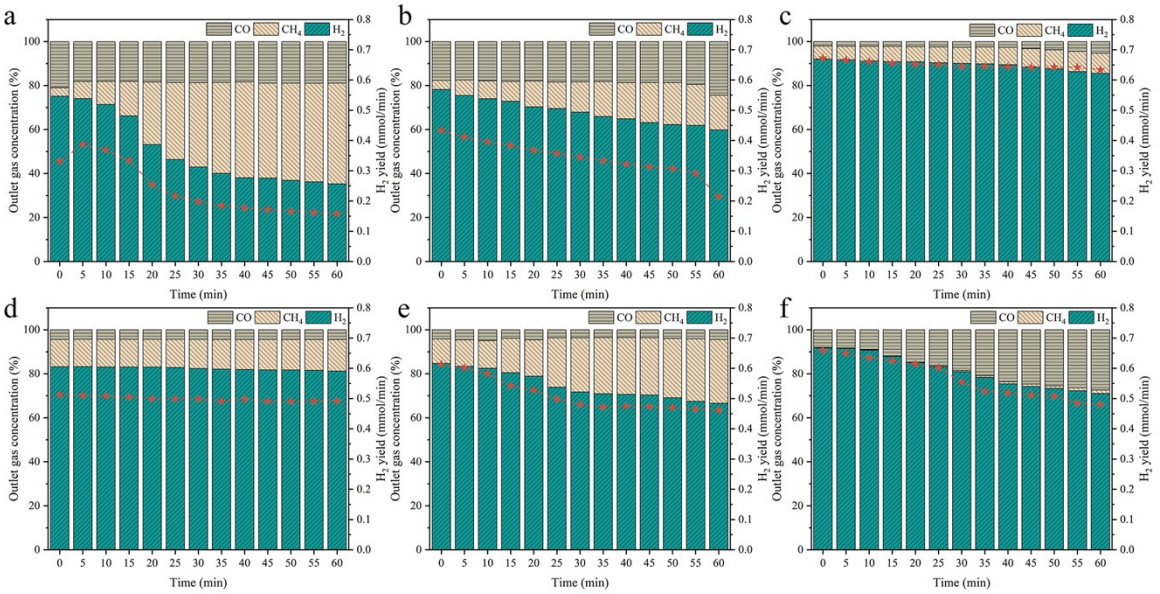

Fig. S9. Outlet gas concentration and H_2 yield of CMD with different temperatures within 60 minutes on reduced Ni1.2Cr2 in a) 650°C; b) 700°C; c) 750°C; d) 800°C; e) 850°C; f) 900°C.

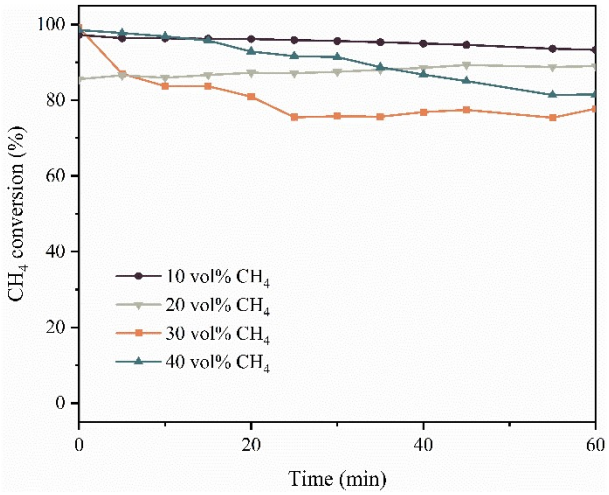

Fig. S10. CH_4 conversion at different methane flows. Reaction conditions: gas flow rate 50 mL min^{-1}, GHSV=3000 h^{-1}.

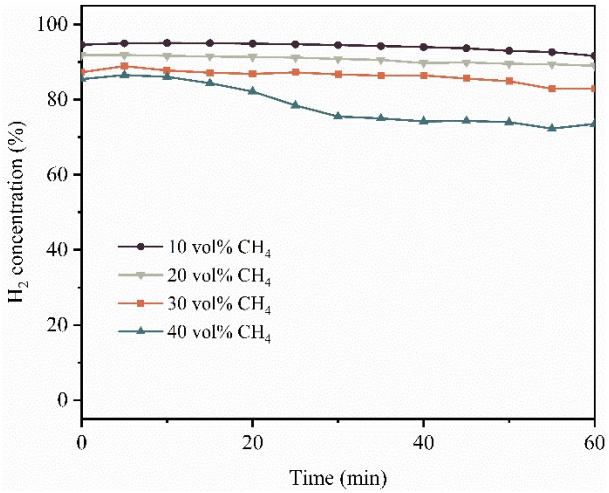

Fig. S11. H_2 concentration at different methane flows. Reaction conditions: gas flow rate 50 mL min^{-1}, GHSV=3000 h^{-1}.

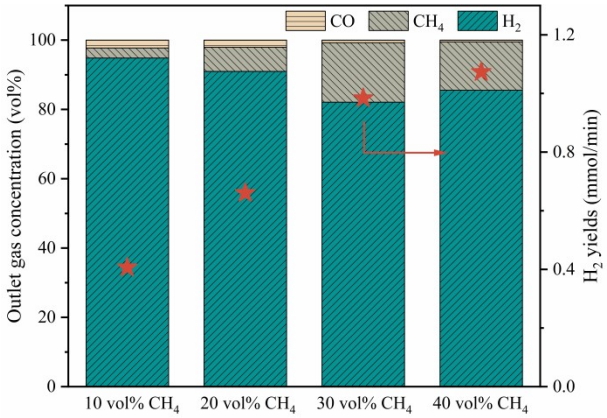

Fig. S12. Outlet gas concentrations and H_2 yields at 20 minutes at different methane flows. Reaction conditions: gas flow rate 50 $mLmin^{-1}$, GHSV=3000 h^{-1}.

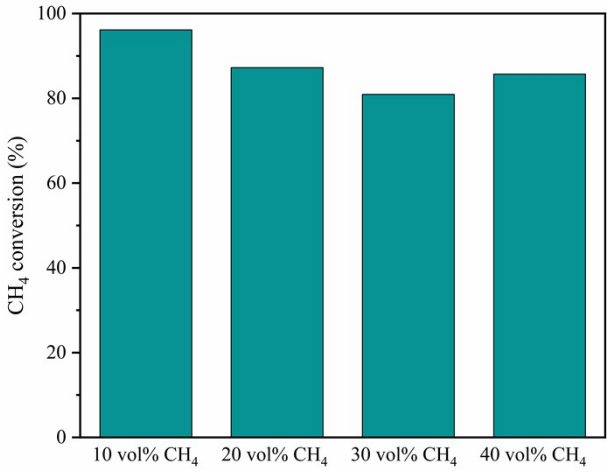

Fig. S13. CH_4 conversion at 20 minutes at different methane flows. Reaction conditions: gas flow rate 50 mL min^{-1}, GHSV=3000 h^{-1}.

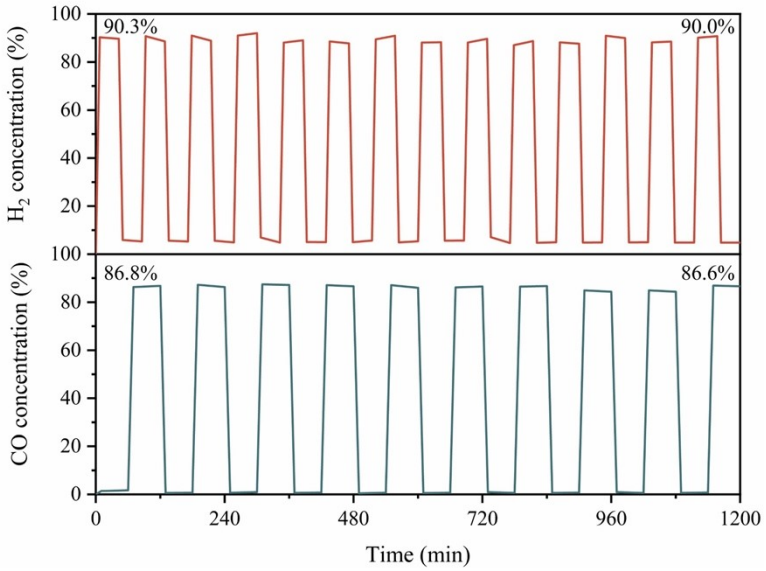

Fig. S14. Cyclic stability test of reduced Ni1.2Cr2: a) H_2 concentration during 10 cycles; b) CO concentration during 10 cycles.

Characterizations of the reacted catalysts

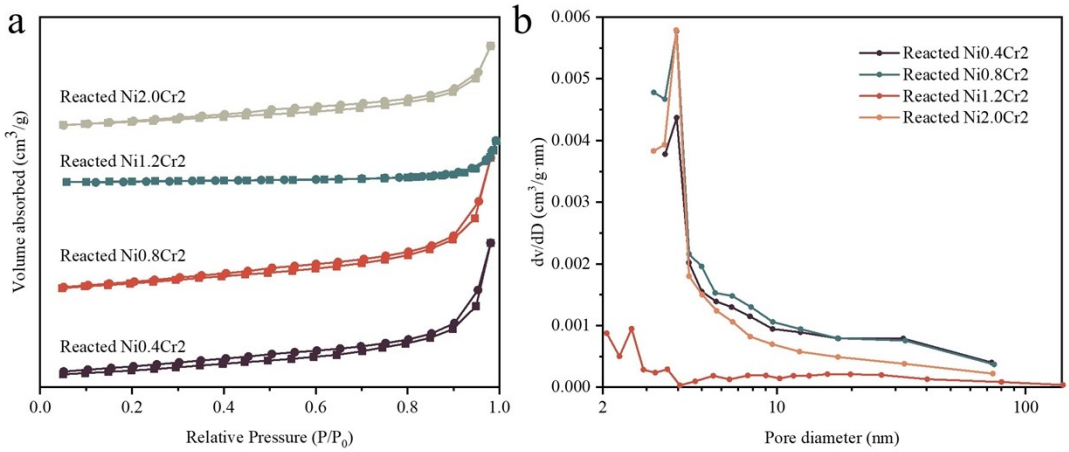

Fig. S15. a) N_2 adsorption/desorption isotherms of reacted Ni*x*Cr2 catalysts; b) Pore size distributions of reacted Ni*x*Cr2 catalysts.

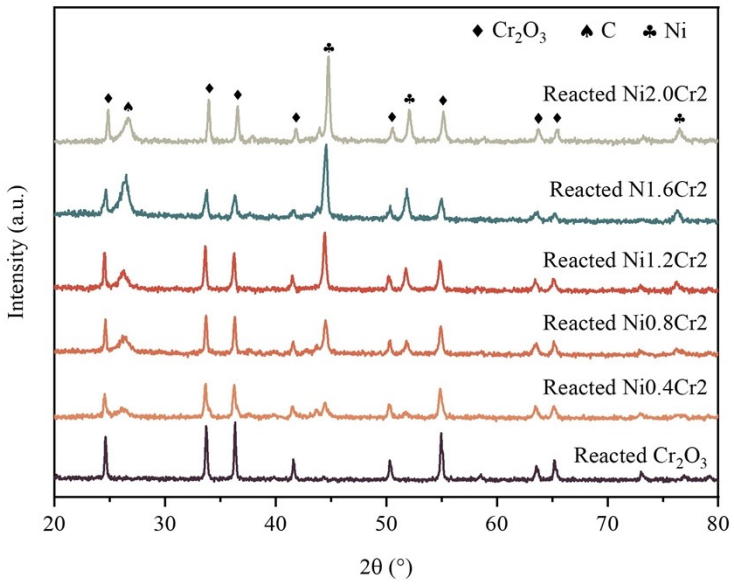

Fig. S16. XRD patterns of the reacted Ni*x*Cr2 catalysts with different Ni/Cr ratios.

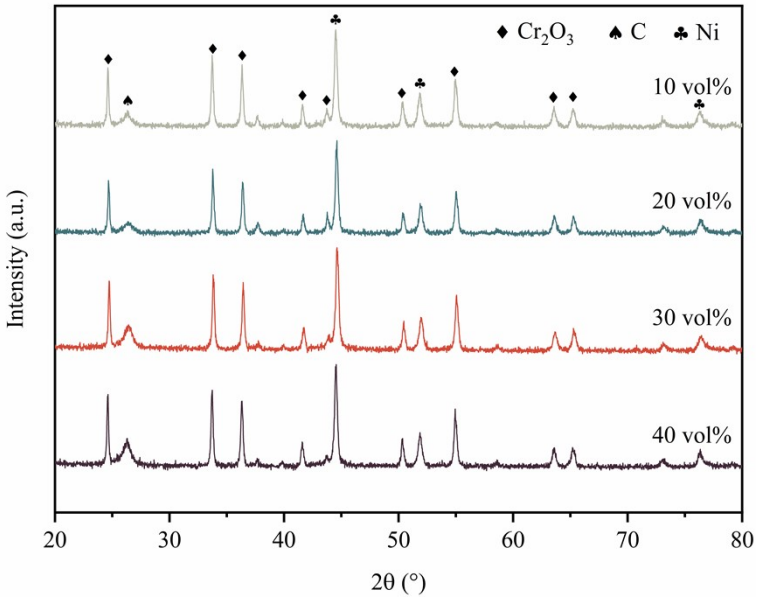

Fig. S17. XRD patterns of the reacted Ni1.2Cr2 at different methane concentrations.

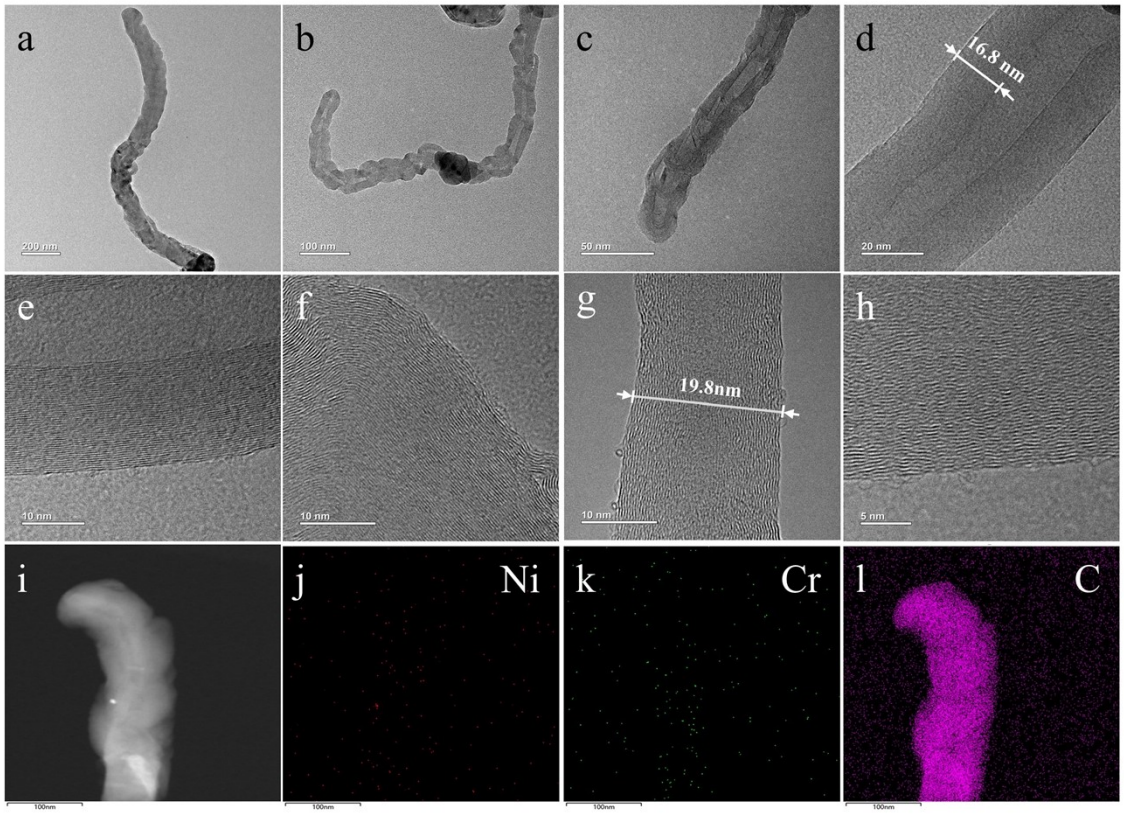

Fig. S18. TEM images of the 1 h reacted Ni1.2Cr2 at 750°C.

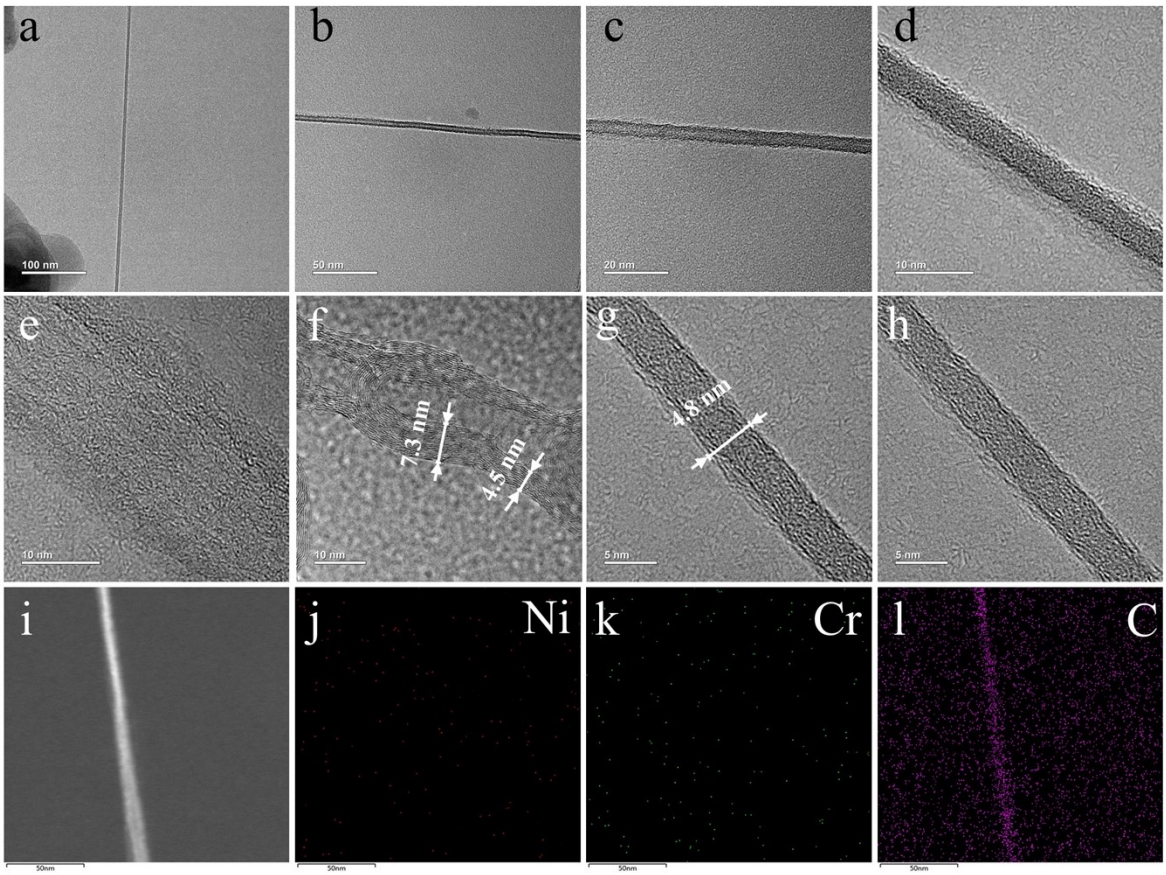

Fig. S19. TEM images of the 1 h reacted Ni1.2Cr2 at 800°C.

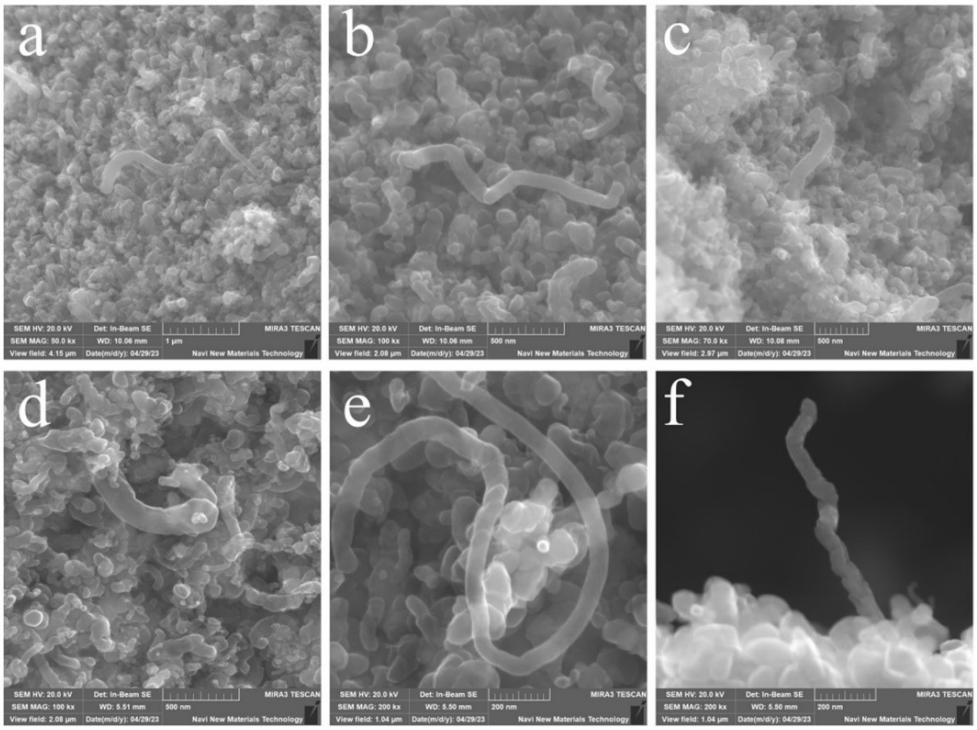

Fig. S20. SEM images of 1h reacted Ni1.2Cr2 catalyst.

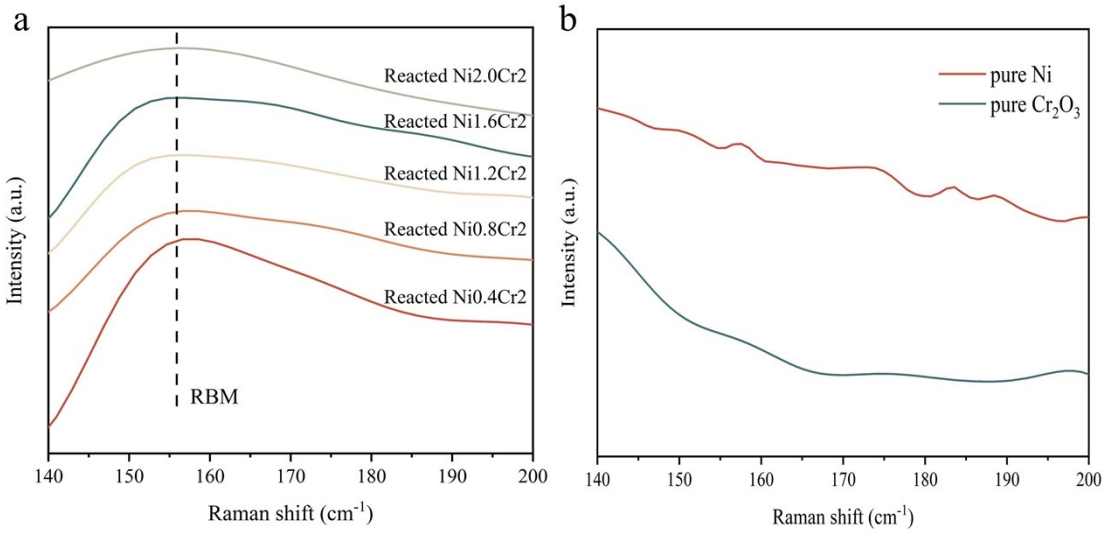

Fig. S21. Raman spectra for a) reacted Ni*x*Cr2 catalysts; b) pure Cr_2O_3 and Ni.

Structure identification and mechanism revelation

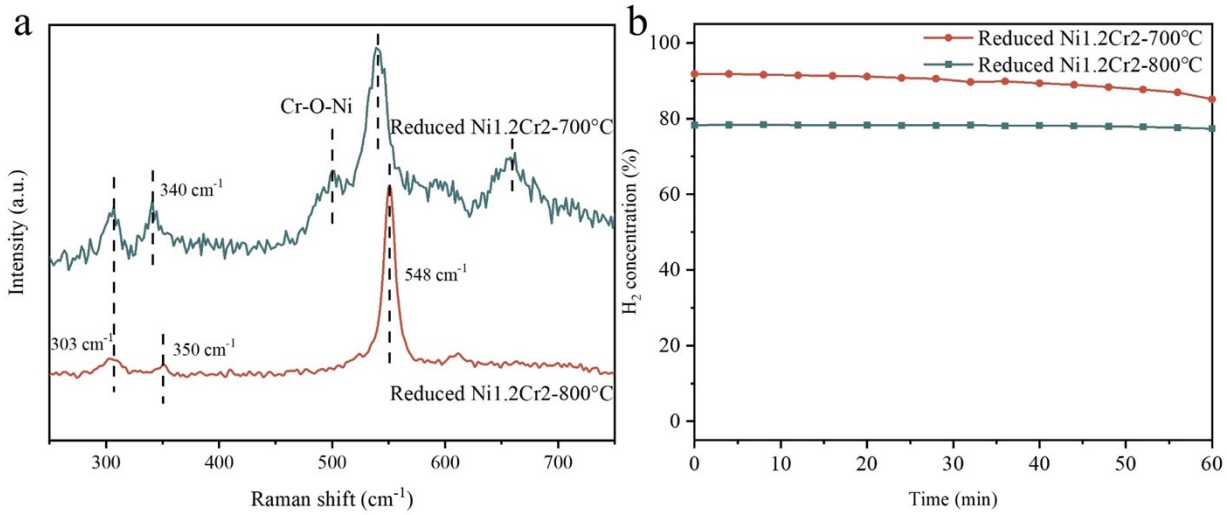

Fig. S22. a) Raman profiles of reduced Ni1.2Cr2 at 700°C and 800°C; b) H_2 concentration on reduced Ni1.2Cr2 at 700°C and 800°C (CMD at 750°C).

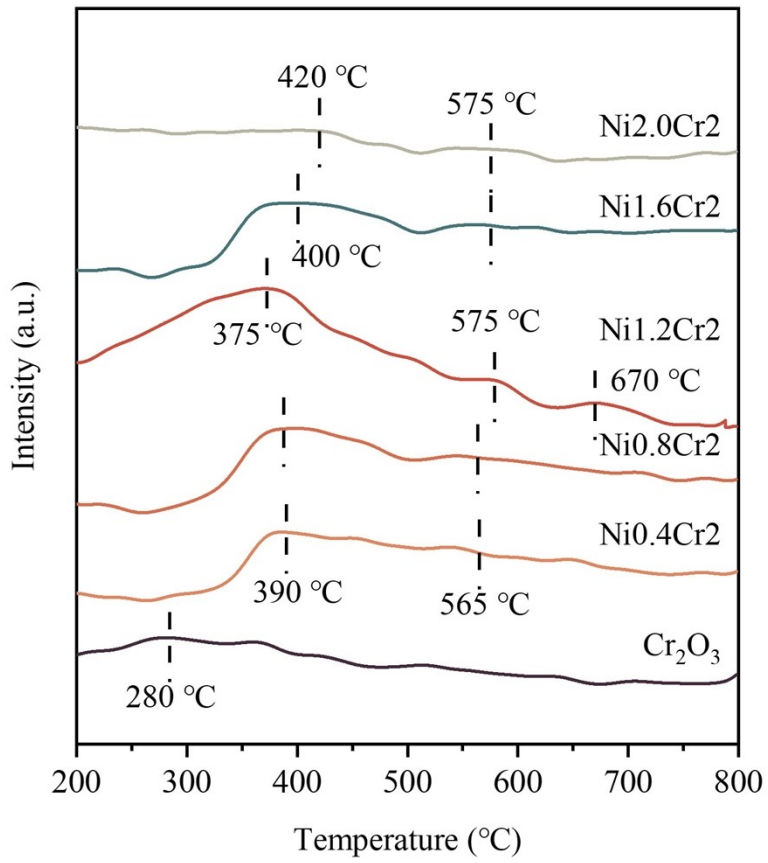

Fig. S23. NH_3-TPD profiles of the reduced Ni*x*Cr2 catalysts with different Ni/Cr ratios.

In the NH_3-TPD spectra of Cr_2O_3, a low temperature peak can be observed at about 280°C, which is attributed to the existence of Lewis acid sites due to the absorbed ammonia on the terminal -OH groups. In addition, as the Ni/Cr ratios gradually increases, moderate- and high-temperature peaks appear, which are assigned to the strong Brønsted acid sites. For reduced Ni1.2Cr2, the temperature peak shifted to 375°C, indicating the enhancement in the combining capability between –OH and ammonia. This could be attributed to the formation of the Cr-O-Ni structure. Additionally, the peaks located at 575°C and 670°C were clearly observed, which was assigned as the strong Brønsted acid sites at the surface of the reduced Ni1.2Cr2. This could be the dominant for methane activation. Meanwhile, the total capacity of NH_3 adsorbed can be calculated by integrating the NH_3-TPD spectrum. It is found that the integral area of the reduced Ni1.2Cr2 is much larger than those of other catalysts, thus performing highly activated performance on CMD.

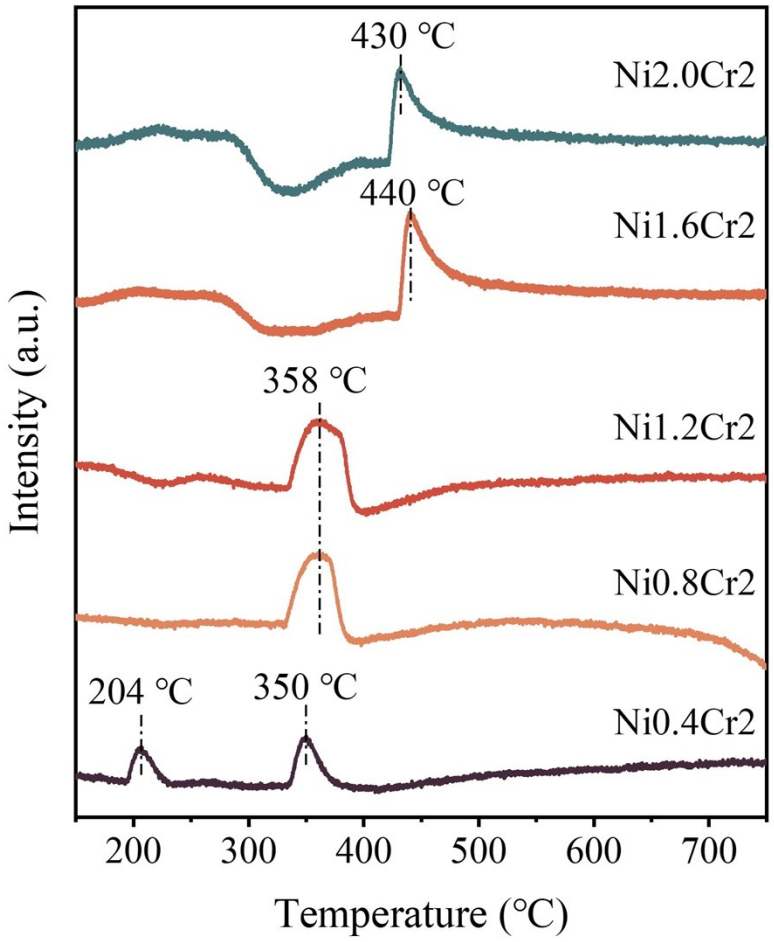

Fig. S24. H_2-TPD profiles of the reduced catalysts with different Ni/Cr ratios.

The peak shifted to higher temperatures with the increase in the Ni/Cr ratios. This phenomenon may be due to the strong adsorption of hydrogen on the catalyst surface, or the desorption of hydrogen tightly bound to the catalyst matrix or the escaped hydrogen, which would improve hydrogen storage capacity. Meanwhile, integrating the catalysts of various proportions, the integrated area of reduced Ni1.2Cr2 is larger than the rest of the catalysts. The surface has higher nickel dispersion, and more surface dissociated hydrogen is formed on the catalyst. It indicates that the addition of nickel is closely related with the H_2 chemisorption ability in the process of CMD.

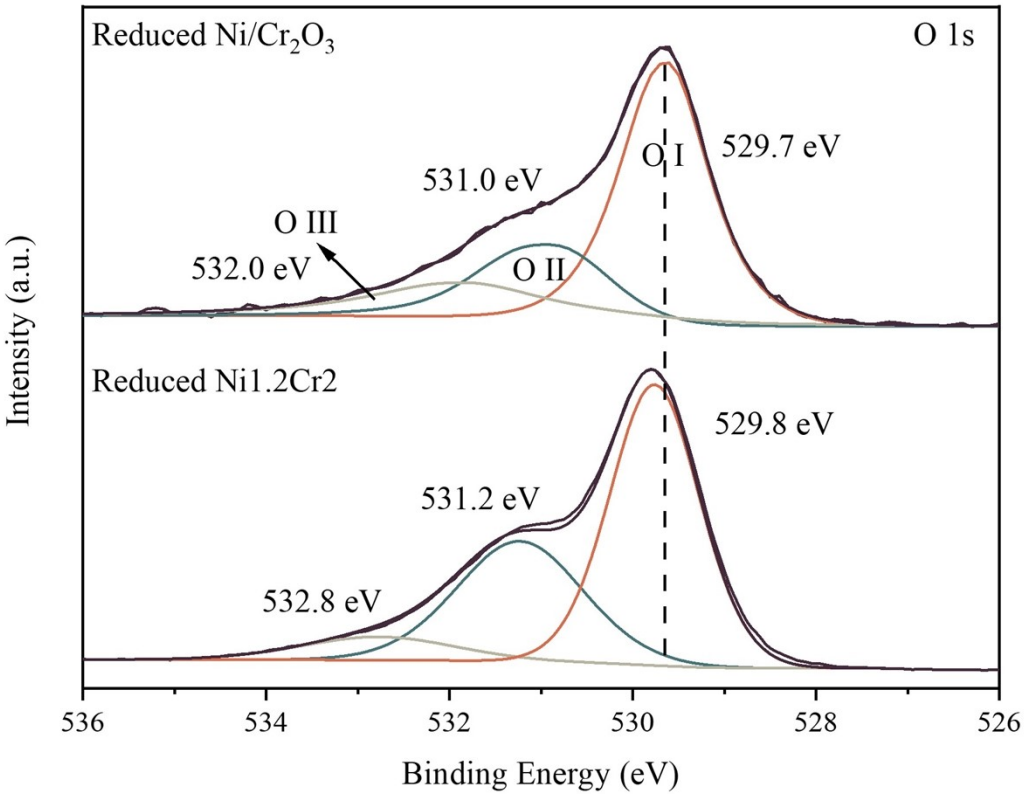

Fig. S25. XPS O 1s spectra of the reduced Ni1.2Cr2 and Ni/Cr_2O_3 catalysts.

The O 1s spectra of the reduced Ni1.2Cr2 and Ni/Cr_2O_3 catalysts are shown in Fig. S25. The O 1s spectra were divided into three peaks at 529.8 eV (OI), 531.2 eV (OII), and 532.3 eV (OIII), which belong to lattice oxygen, oxygen vacancies, and surface –OH or CO_3^{2-} at the catalyst surface [30], respectively. Specifically, the OI/OII ratios of the reduced NiO/Cr_2O_3 and Ni1.2Cr2 were 2.50 and 1.60, respectively. This demonstrates rich oxygen vacancy beyond the surface of the reduced Ni1.2Cr2 sample. Consequently, the abundant oxygen vacancy formed can effectively promote methane activation and the surface $Ni^{+\delta}$ formed can provide moderate lattice oxygen, thus synergistically promoting methane decomposition.

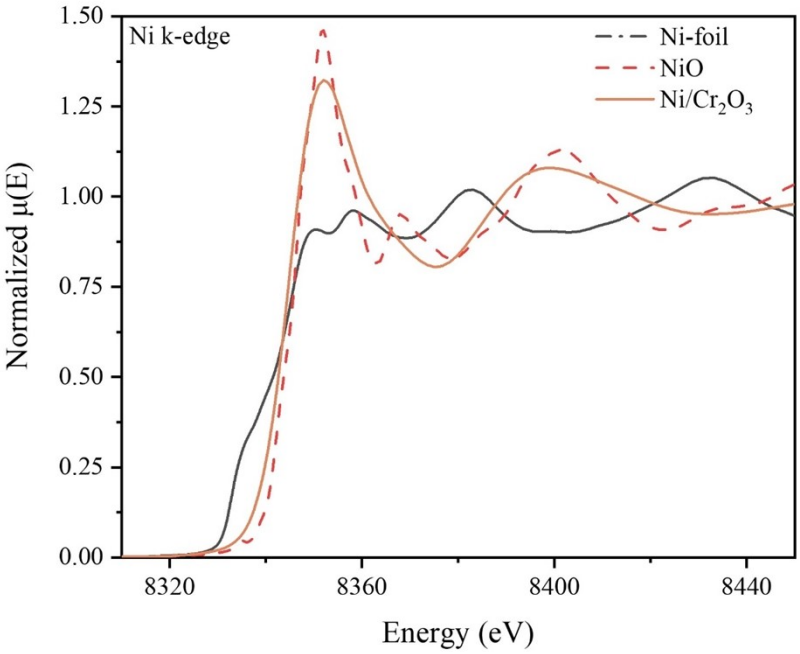

Fig. S26. Ni K-edge XANES spectra of the control group Ni/Cr_2O_3 catalyst and reference samples.

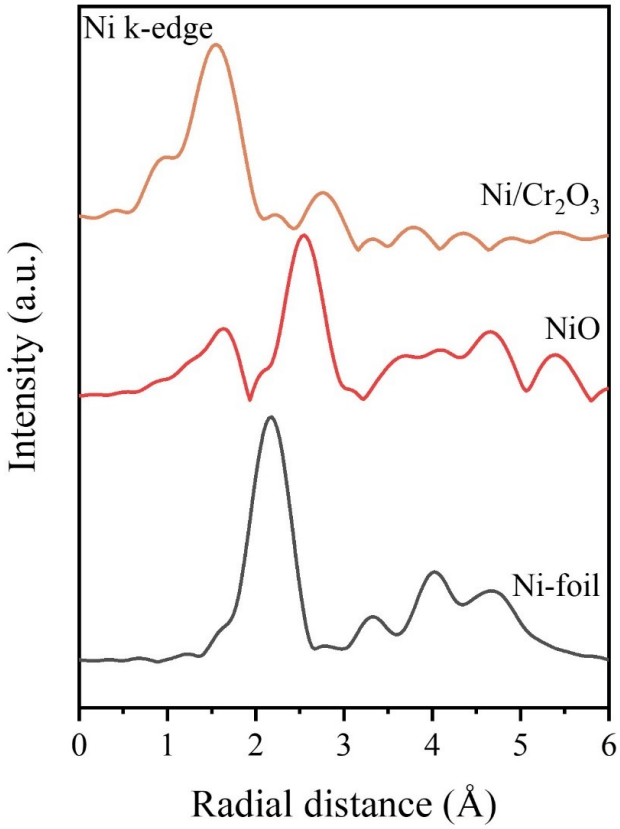

Fig. S27. Fourier transformed (FT) k^3-weighted $\chi(k)$-function of the EXAFS spectra for Ni K-edge of contral group Ni/Cr_2O_3.

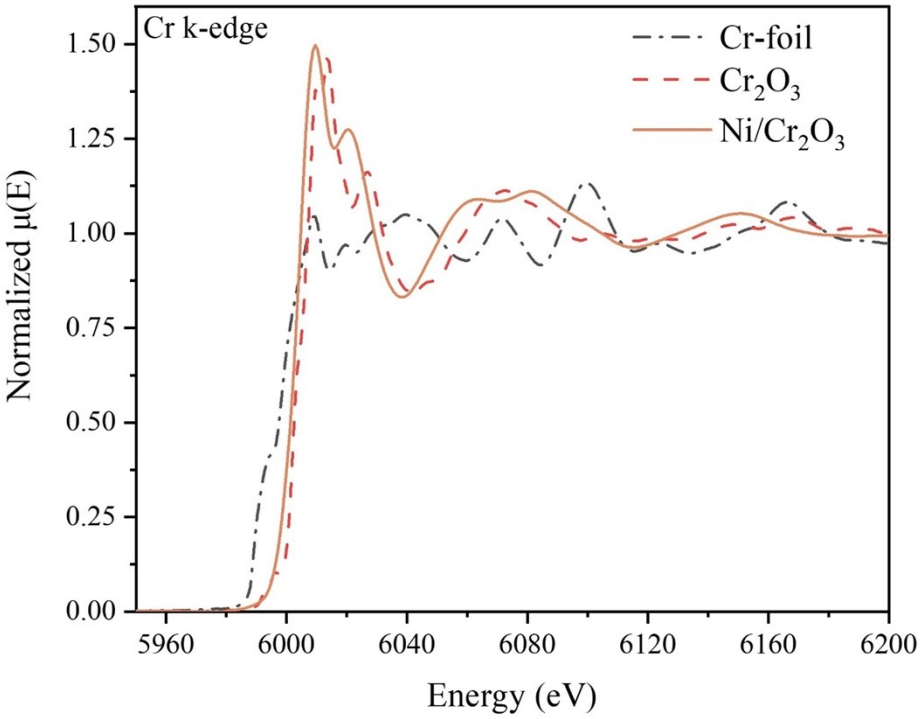

Fig. S28. Cr K-edge XANES spectra of the contral group Ni/Cr_2O_3 catalyst and reference samples.

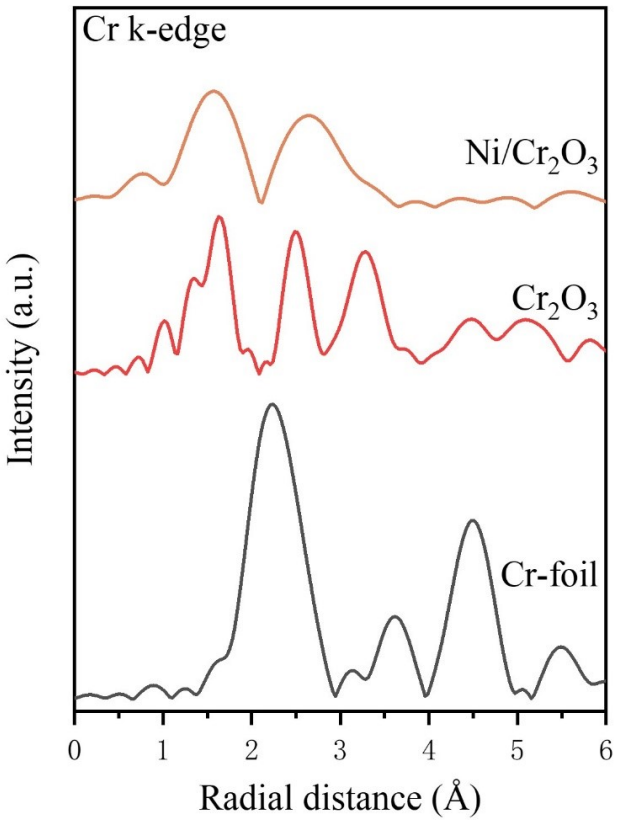

Fig. S29. Fourier transformed (FT) k^3-weighted $\chi(k)$-function of the EXAFS spectra for Cr K-edge of the contral group Ni/Cr_2O_3.

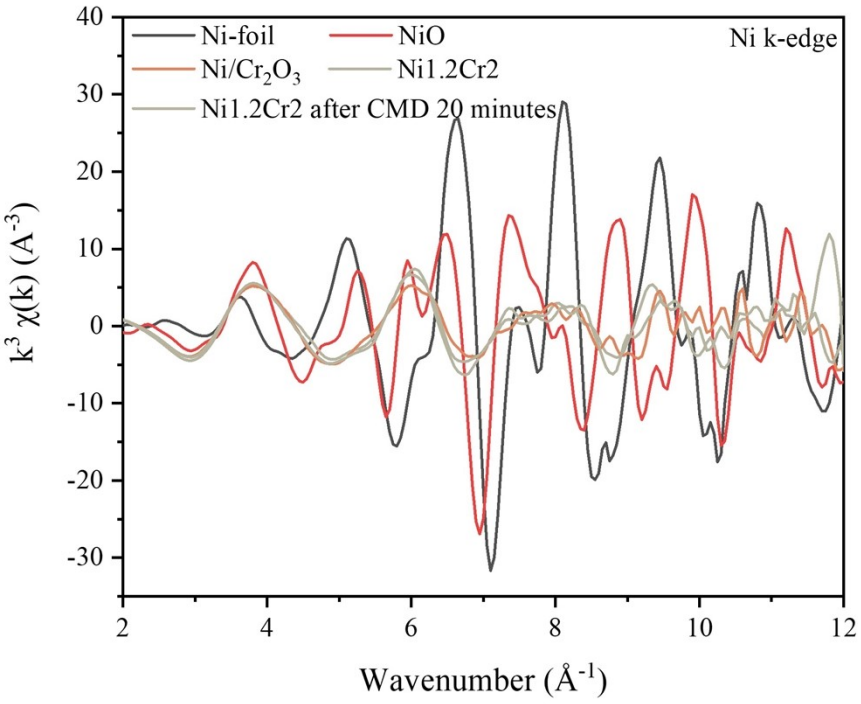

Fig. S30. Ni EXAFS spectra for each sample in k space.

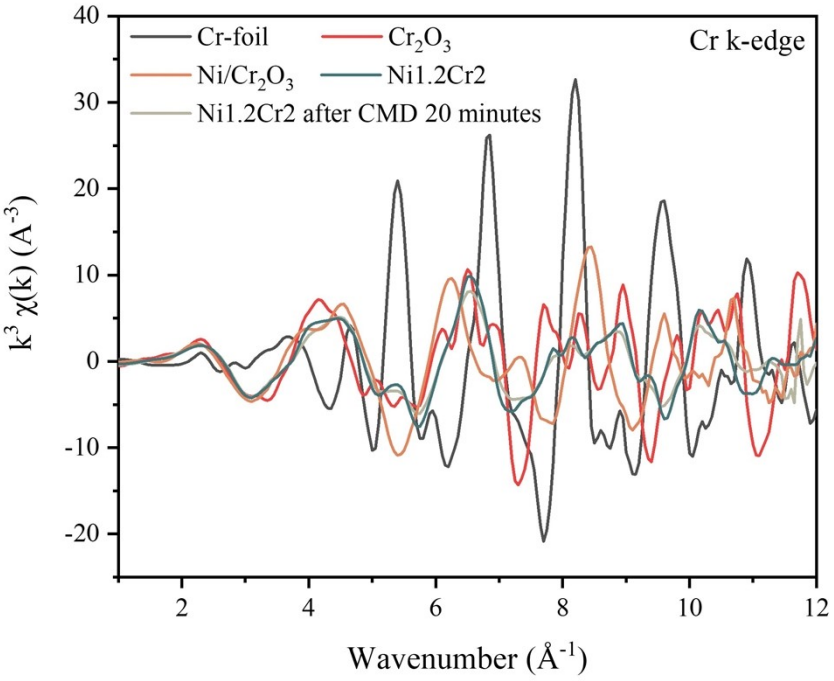

Fig. S31. Cr EXAFS spectra for each sample in k space.

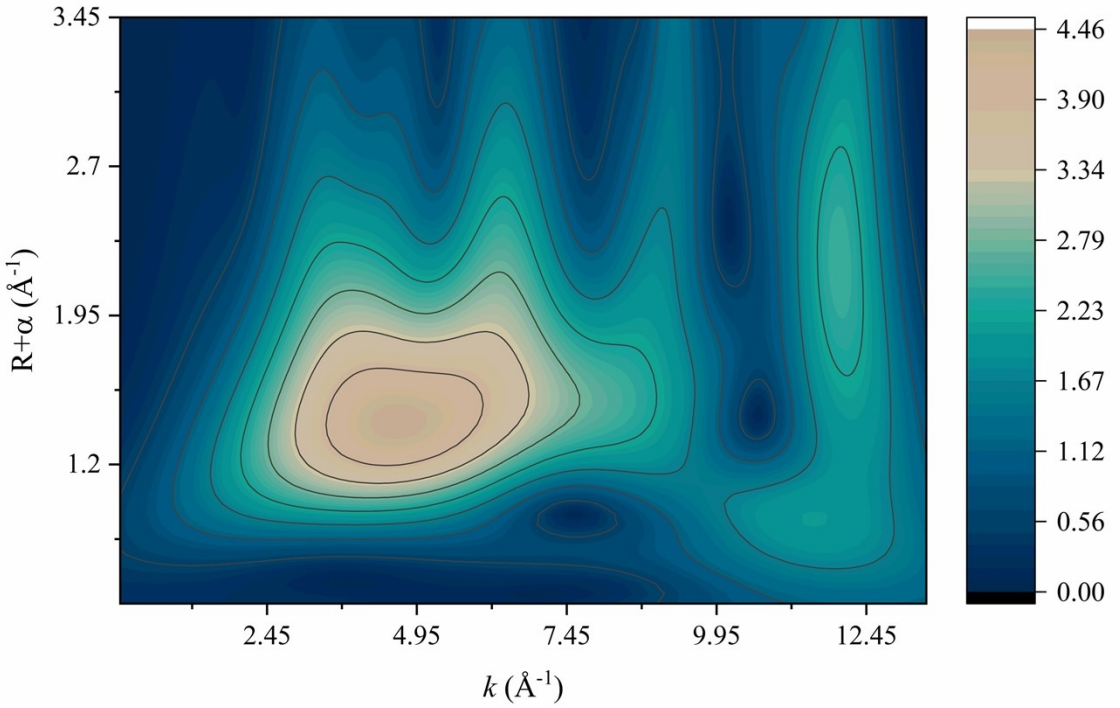

Fig. S32. Wavelet transforms for the k^3-weighted EXAFS signals of Ni for the control group Ni/Cr_2O_3.

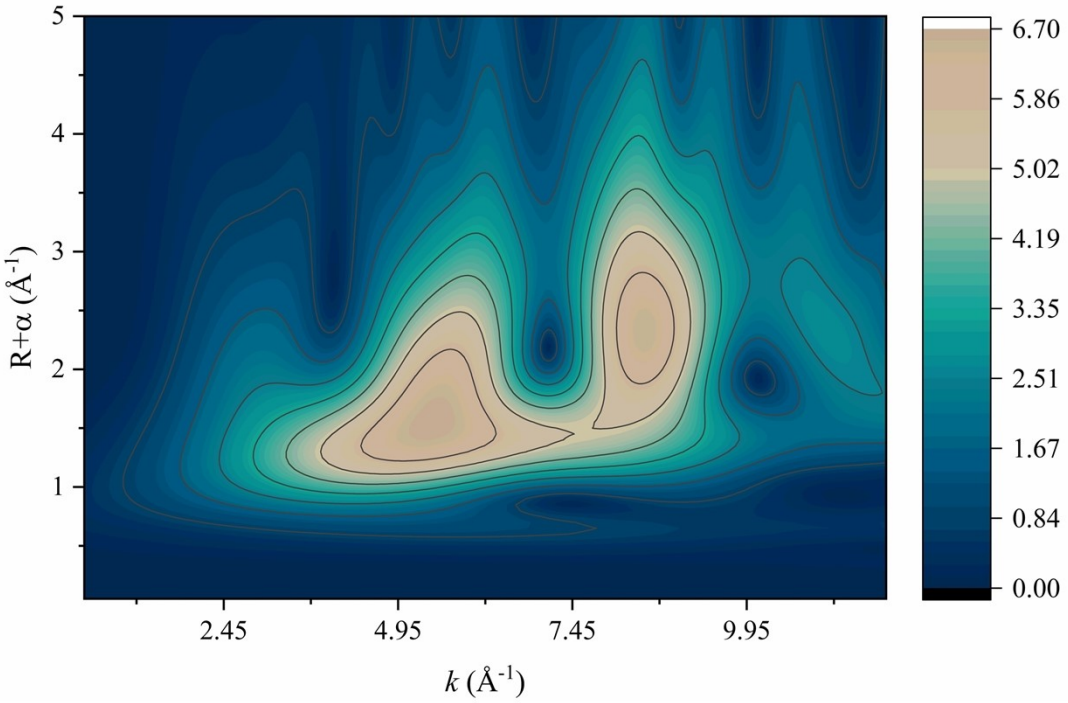

Fig. S33. Wavelet transforms for the k^3-weighted EXAFS signals of Cr for the control group Ni/Cr_2O_3.

DFT calculations

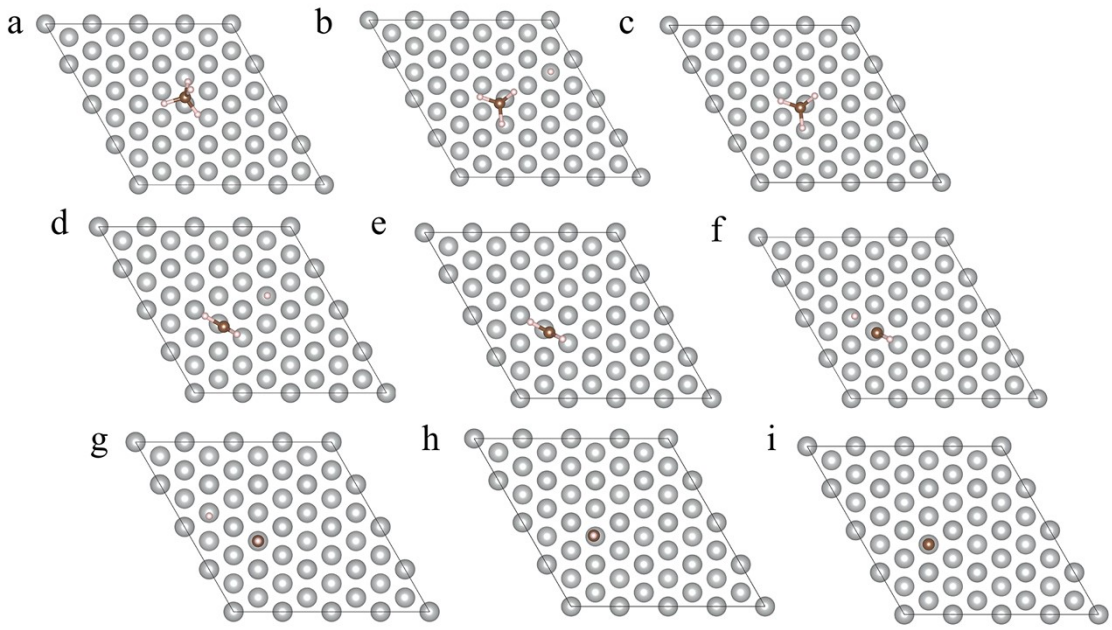

Fig. S34. Transition state images for CMD on Ni surfaces. Spheres: gray= Ni, pink= H, and dark brown= C.

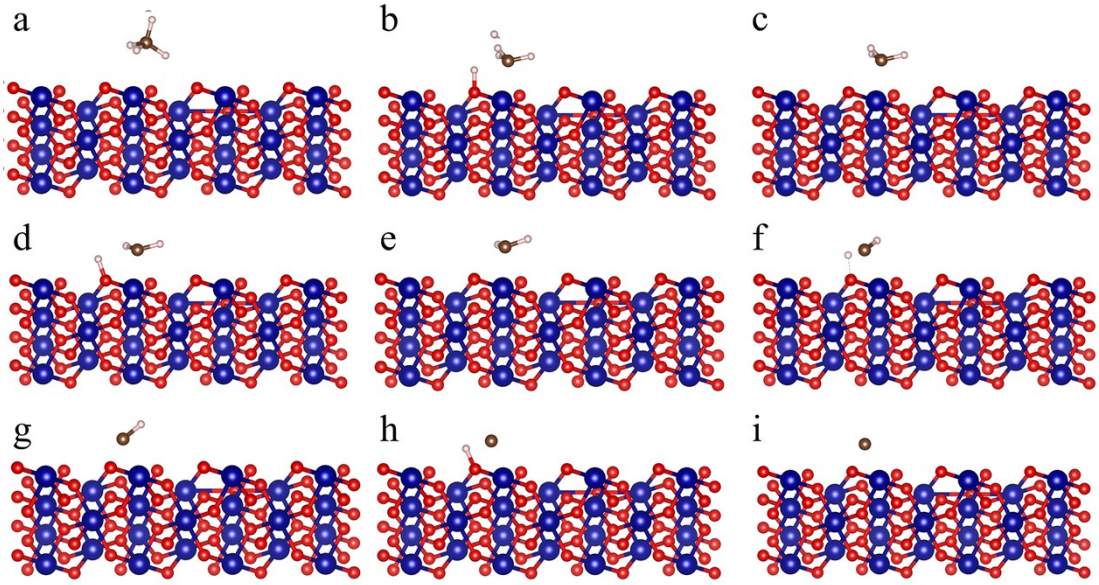

Fig. S35. Transition state images for CMD on Cr_2O_3 surfaces. Spheres: blue= Cr, red= O, pink= H, and dark brown= C.

Table S1. Cell parameters of DFT model.

Sample	Space group	Cell parameters
Ni bulk	$Fm\bar{3}m$	a=b=c=3.835 Å, α=β=γ=90°
Cr_2O_3 bulk	$R\bar{3}c$	a=b=5.03 Å, c=13.702 Å, α=β=90°, γ=120°
Cr_2O_3(012) and Ni@Cr_2O_3(012)		a=13.25700 Å, b=9.30640 Å, c=20.26710 Å, α=β=γ=90°
Ni(111)		a=b=9.75810 Å, c=20.97560 Å, α=β=90°, γ=120°

Table S2. Metal contents of the Ni*x*Cr2 catalysts.

Sample	Theoretical Ni: Cr ratio	Actual Ni:Cr ratio
Ni0.4Cr2	0.20	0.19
Ni0.8Cr2	0.40	0.43
Ni1.2Cr2	0.60	0.56
Ni1.6Cr2	0.80	0.76
Ni2.0Cr2	1.00	1.02

Table S3. Physiochemical properties of the H_2 reduced Ni*x*Cr2 catalysts.

Sample	BET Surface area (m^2/g)	Pore volume (cm^3/g)	Pore diameter (nm)	Ni Crystallite size (nm)[a]
Ni0.4Cr2	7.5	0.027	14.5	24.3
Ni0.8Cr2	6.4	0.022	13.5	25.2
Ni1.2Cr2	4.9	0.020	16.9	22.6

Ni2.0Cr2	4.5	0.016	14.4	35.8

[a] Determined by Scherrer's equation.

Table S4. Summary of BET characteristics of the 1h reacted Ni1.2Cr2 catalysts.

Sample	BET Surface area (m^2/g)	Pore volume (cm^3/g)	Pore diameter (nm)
reacted Ni0.4Cr2	18.3	0.066	14.5
reacted Ni0.8Cr2	21.5	0.067	12.5
reacted Ni1.2Cr2	15.4	0.064	16.6
reacted Ni2.0Cr2	14.3	0.040	11.4

Table S5. Summary of XPS characteristics of reduced Ni1.2Cr2 and Ni/Cr_2O_3 catalysts.

Sample	OI	OII	OIII	OII/OI
reduced Ni1.2Cr2	0.56	0.35	0.09	0.63
reduced Ni/Cr_2O_3	0.60	0.24	0.16	0.40

Table S6. The coordination parameters of Ni for investigated samples

Sample	Coordination type	Coordination number	R (Å)	σ^2	ΔE (eV)	R-factor
Ni-foil	Ni-Ni	12	2.48	0.00627	6.39	0.23%
NiO	Ni-Ni	12	2.95	0.00710	4.23	0.15%
	Ni-O	6	2.07	0.00705	5.34	
Ni/Cr_2O_3	Ni-O	5.6	1.89	0.00300	15	3.30%
	Ni-Cr	3.5	2.03	0.00300	6	

	Ni-Ni	2.3	3.38	0.00300	6	
reduced Ni1.2Cr2	Ni-O	7.9	1.93	0.00300	15	6.91%
	Ni-Cr	2.5	2.90	0.00300	6	
	Ni-Ni	2.9	3.43	0.00300	6	

Table S7. The coordination parameters of Cr for investigated samples

Sample	Coordination type	Coordination number	R (Å)	σ^2	ΔE (eV)	R-factor
Cr-foil	Cr-Cr	12	12	0.00300	1.21	1.28%
Cr_2O_3	Cr-O	9.2	1.99	0.00260	0.67	0.72%
	Cr-Cr	1.5	2.63	0.00330	7.56	
	Cr-Cr	5.2	2.89	0.00300	5.68	
Ni/Cr_2O_3	Cr-O	10.9	1.99	0.00300	0.21	0.24%
	Cr-Cr	2.0	3.11	0.00300	25.83	
	Cr-Ni	12.8	3.31	0.00300	32.54	
reduced Ni1.2Cr2	Cr-O	8.8	1.97	0.00300	2.38	1.48%
	Cr-Cr	3.3	2.86	0.00300	16.58	
	Cr-Ni	2.3	3.39	0.00300	1.0	

Table S8. Transition state results of methane decomposition on Ni(111), Cr_2O_3(012), and Ni(111)/Cr_2O_3(012)

Reaction	Reaction barrier(eV)		
	Ni(111)	Cr_2O_3(012)	Ni(111)/Cr_2O_3(012)
$CH_4(g) \rightarrow CH_4^*$	-0.24	-0.13	-0.19
$CH_4^* \rightarrow$TS-1	0.63	0.76	0.42
TS-1$\rightarrow CH_3^*$	-0.86	-0.86	-0.64
$CH_3^* \rightarrow$TS-2	0.57	0.91	0.26

TS-2→CH_2*	-0.90	-1.48	-0.69
CH_2*→TS-3	0.49	0.95	0.35
TS-3→CH*	-0.81	1.07	-0.69
CH*→TS-4	0.20	0.29	0.36
TS-4→C*	-0.65	-0.67	-0.82